5-2019

Comparison of Induced and Parasitic Drag on Wings with Minimum Induced Drag

Sarah A. Abdel-Motaleb
Utah State University

COMPARISON OF INDUCED AND PARASITIC DRAG

ON WINGS WITH MINIMUM INDUCED DRAG

by

Sarah A. Abdel-Motaleb

A project submitted in partial fulfillment
of the requirements for the degree

of

MASTER OF SCIENCE

in

Mechanical Engineering

Approved:

Douglas Hunsaker, Ph.D. Major Professor	Robert Spall, Ph.D. Committee Member
Thomas Fronk, Ph.D. Committee Member	

UTAH STATE UNIVERSITY
Logan, Utah

ABSTRACT

Comparison of Induced and Parasitic Drag on A Wing with Minimum Induced Drag

by

Sarah Abdel-Motaleb, Master of Science

Utah State University, 2018

Major Professor: Dr. Douglas Hunsaker
Department: Mechanical Engineering

Minimizing the induced drag for steady level flight is a variational problem that requires solving for the optimum lift distribution given a set of design constraints. From lifting-line theory, minimizing the induced drag is, in part, achieved by varying the Fourier coefficients used to describe the section lift. The elliptic lift distribution minimizes the induced drag for a wing with fixed weight and wingspan by setting all but the first coefficient to zero. If wingspan is allowed to vary, a negative third Fourier coefficient is utilized to reach an optimum lift distribution that further reduces the induced drag for stress-limited designs. However, to produce an optimal section-lift distribution for minimum induced drag, the wing is required to vary twist along the span, which contributes to the parasitic drag component and may compromise the benefits gained from minimizing the induced drag. Here, the effect of these lift distributions on the parasitic drag is investigated. It is shown that twisting the wing to produce optimal lift distribution that minimizes induced drag can increase the parasitic drag values enough to nearly cancel or surpass the benefits gained by the reduction of the induced drag depending on the aircraft and flight conditions. One aircraft example is studied. Other aircraft might have different results.

(50 pages)

ACKNOWLEDGMENTS

I am heartily grateful to my supervisor, Dr. Douglas Hunsaker, for his keen interest in my academic and personal improvement, guidance and mentorship from the initial to the final level of this project.

I would like to extend my gratitude to my committee members, Dr. Thomas Fronk and Dr. Robert Spall for their support and encouragement. I am grateful to Dr. Mac McKee and Dr. Calvin Coopmans for their guidance, helpful comments and their support getting the project started.

I would like to also thank my colleagues in AeroLab and AggieAir lab for their endless feedback and support. I am grateful to Nathan Hoffer, Jeffrey Taylor, Joshua Hodson and Zachary Montgomery for all the time and effort they put in to help me. I must also express my gratitude to Chritine Spall, Lindi Brown, Karen Zobell and all the staff for their help and time.

I would like to express my profound gratitude to my parents, family and friends for their continuous support and encouragement throughout my degree. This project is theirs as much as it is mine. Finally, my thanks go to the Utah Water Research Lab for funding this project.

Sarah Abdel-Motaleb

CONTENTS

LIST OF TABLES

Table Page

LIST OF FIGURES

NOMENCLATURE

A	=	beam cross sectional area
A_n	=	n^{th} Fourier coefficient in lifting-line solution for the section-lift distribution
B_n	=	n^{th} Fourier coefficient in lifting-line solution for the dimensionless section-lift distribution
AR	=	wing aspect ratio
b	=	wingspan
C_{D_0}	=	section parasitic drag coefficient at zero lift
C_{D_1}	=	section parasitic drag linear coefficient
C_{D_2}	=	section parasitic drag quadratic coefficient
C_{D_i}	=	induced drag coefficient
C_{D_p}	=	Total parasitic drag coefficient
$\tilde{C}_{D_p}$	=	section parasitic drag coefficient
C_L	=	wing lift coefficient
C_m	=	pitching moment coefficient
C_σ	=	shape coefficient for stress-limited design
c	=	local wing section chord length
D_i	=	wing total induced drag
h	=	height of the beam cross section
I	=	beam area moment of inertia
L	=	wing total lift
$\tilde{L}$	=	wing section lift
$\tilde{M}_b$	=	wing section bending moment
n	=	Fourier coefficient index in lifting-line solution for the section-lift distribution
S	=	wing planform area
S_b	=	wing section structural weight to section bending moment proportionality constant
t_{max}	=	maximum section airfoil thickness
V_∞	=	freestream airspeed
W	=	total aircraft weight
W_n	=	total aircraft non-structural weight
W_r	=	non-structural weight at the wing root
W_s	=	total wing structural weight
$\tilde{W}_n$	=	spanwise section wing non-structural weight
$\tilde{W}_s$	=	spanwise section structural weight
z	=	spanwise coordinate relative to the midspan, positive out left wing
γ	=	beam material specific weight
δ	=	Parabolic flap deflection
θ	=	change of variables for the spanwise coordinate
ρ	=	air density
σ_{max}	=	beam material maximum longitudinal stress

CHAPTER ONE

INTRODUCTION

The reduction of drag for finite wings has been the focus of many research efforts in a strong attempt to increase the efficiency, and thus reduce the economic and environmental impact, of aircraft. In comparison with other types of transportation fuel, jet fuel takes up a major portion of the total fuel consumption and is expected to grow by 64% from 2017 to 2050 according to the last annual energy outlook report of U.S. Energy Information Administration (EIA) [1]. As per the Bureau of Transportation Statistics (BTS), U.S. passenger airlines' collective net profit increased by 18.1 billion dollars in 2015 [2] mostly due to lower kerosene-based aviation fuel expenses in 2015 as compared to 2014. More efforts are directed to increasing the overall efficiency of aircraft to not only reduce costs but to also comply with the continuously updated environmental policies and emission regulations. Excluding endeavors to increase the operational efficiency of aircraft and especially the commercial ones like optimizing the speeds and use of space of aircraft, reducing the drag acting on the aircraft has been an area of interest of many research topics concerned with flight efficiency. For subsonic flight speeds, major contributors to total aircraft drag are viscous or parasitic drag and induced drag or drag due to lift. The total drag on an aircraft can be described as

$$C_D = C_{D_p} + C_{D_i}$$

where the first term represents the parasitic or viscous drag and the second term describes the drag due to lift. Efforts as early as 1930s have focused on reducing the viscous drag component [3]. Solutions based on controlled pressure gradients, suction, reduction of surface roughness and wetted area, and others are well documented in many research and survey works like [4,5]. As shown from Eq. (1), the induced drag varies with the lift produced by the aircraft wing. Throughout the flight profile, induced drag constitutes 40% to 50% of the total drag on the aircraft [6,7]. While a lower lift coefficient/weight and longer spans intuitively can help reduce the drag due to lift, the fact that many aircraft missions require higher lift coefficient/payload, i.e. take-off or landing where induced drag could reach 90% of total drag [8], and the structural and space limitations on wing geometries highlight the need to further investigate new methods to reduce drag due to lift. Induced drag is a bi-product of the lift generated on a 3D wing. When the aircraft speeds up and assumes an angle of attack to the freestream air, the wing experiences a pressure difference between its upper and lower surfaces, generating the lift forces that lift the aircraft body. The same pressure difference

across the upper and lower surfaces of the wing force the air at the tips of the wing to escape from the bottom to the top of the wing. Joined by the freestream, the air sliding from beneath the wing to regions of lower pressure above the wing forms a line of vortices downstream which affect the angle of attack of the wing as they form in a line inclined to the freestream flow direction. This results in a component of the lift forces in the horizontal direction that is called "drag due to lift".

The relationship between drag and lift was referred to in early aerodynamics research like [9,10] that pointed to a possible relation between the aspect ratio and drag due to lift. In 1907, Lanchester [11] mentioned the phenomenon of the vortex wake and suggested further investigation of its effects. Then in 1918, Prandtl [12,13,14] introduced the lifting-line theory which not only predicts the section lift on a wing with a given twist distribution but also provides a model that calculates the induced drag given a lift distribution. One approach to reduce the induced drag on a wing is preventing or reducing the formation of the vortices at the wing-tips by adding winglets, suction devices or using vertical wings or joined wing/tail set ups to eliminate the vortices or recover thrust power from the formed vortices like in [15,16]. Structural and manufacturing considerations make some of such solutions difficult to incorporate in the aircraft design process [3].

From lifting-line theory's definition of induced drag, Prandtl [12,13,14] was able to minimize the induced drag on a wing using an elliptic lift distribution along the wingspan. Later, Prandtl [17] mentioned that elliptic drag only minimizes the induced drag for a wing with a prescribed total weight and wingspan. He arrived at a bell-shaped lift distribution along the wingspan that minimizes the induced drag for a wing with a fixed total weight and moment of inertia. The new lift distribution shifted the lift forces towards the center of the wing and offered less induced drag than the elliptic lift distribution due to an increase in wingspan. Other research [18-21] follows a similar approach as Prandtl's [17] to minimize the induced drag by varying the lift distribution over wings with different sets of constraints. Hunsaker, Phillips and Joo [21] relaxed Prandtl's constraints in [17] and, following the same analytical procedure, solved for optimal lift distribution that minimizes the induced drag for different sets of constraints. They arrived at an optimal lift distribution that produces less induced drag than Prandtl's [17] bell shaped lift distribution under certain conditions. It's important to note that changing the lift distribution over a wing requires altering its sectional twist, affecting the viscous drag profile of the wing. This work investigates the effect of lift distributions aiming to minimize the induced drag on the parasitic drag and total drag for a given wing. In the following sections of this chapter,

Prandtl's [17] and Hunsaker et al.'s [21] analytical procedures are laid out then a numerical algorithm that extends both analytical procedures [22] is discussed.

1.1. Analytical Theory

The lifting-line theory [12-14] provided an early analytical description of induced drag as a function of the total lift produced by a finite wing with no sweep and aspect ratio greater than 4. Prandtl described the circulation distribution along the wingspan in terms of a Fourier sine series [12-14]. Combining this series with the Kutta-Joukowski theorem [23,24] he arrived at the spanwise lift distribution

$$\tilde{L}(\theta) \;=\; 2\rho V_\infty^2 b \sum_{n=1}^{\infty} A_n \sin(n\theta); \;\; \theta \;\equiv\; \cos^{-1}(-2z/b) \tag{1}$$

The lifting-line theory accounts for the first analytical method to compute the required spanwise twist distribution for a finite wing with no sweep or dihedral given a section lift distribution along the wingspan. Using the definition of the lift coefficient and noting that the aspect ratio is defined as

$$AR = b^2/S$$

The total lift can be written as a function of the first Fourier coefficient of the sine series

$$L \;=\; \frac{1}{2}\pi\rho b^2 V_\infty^2 A_1 \tag{2}$$

Using the definitions of the wing aspect ratio and drag coefficient, the induced drag from lifting-line theory, is

$$D_i \;=\; \frac{2(L/b)^2}{\pi\rho V_\infty^2} \sum_{n=1}^{\infty} n \frac{A_n^2}{A_1^2} \tag{3}$$

For convenience, Eq. (1) is rewritten as

$$\tilde{L}(\theta) \;=\; 2A_1\rho V_\infty^2 b\left[\sin(n\theta) + \sum_{n=2}^{\infty} B_n \sin(n\theta)\right]; \quad B_n \equiv \frac{A_n}{A_1}, \quad \theta \equiv \cos^{-1}(-2z/b) \tag{4}$$

Noting that for steady level flight, the lift becomes equal to the total aircraft weight, the induced drag can then be written as

$$D_i \;=\; \frac{2(W/b)^2}{\pi\rho V_\infty^2}\left[1 + \sum_{n=2}^{\infty} nB_n^2\right] \tag{5}$$

It's conspicuous from Eq. (5) that reducing the induced drag is achieved by increasing the span, decreasing the total weight and/or setting all B_n coefficients to zero. However, once the wing structure is considered, changing any of these design variables affects the other two, compromising the benefits intended. For instance, increasing the wingspan increases the total weight, which increases the induced drag. This recursive dependency and variational problem highlight the difficulty of solving for the optimum wing design for minimum induced drag without placing any constraints on either the weight or lift, their distributions and/or the wingspan. Prandtl was the first to discuss this problem in 1933 [17]. He mentioned, in the same paper, that the elliptic lift distribution [12-14], where all B_n are set to zero, is not always the optimum lift distribution for minimum induced drag, but rather for minimum induced drag for a wing with constant weight and wingspan. Fixed wingspan and aircraft total weight are not necessarily the ideal set of constraints in the wing design process. Prandtl [17] suggested a structural weight distribution that accounts for the bending moments on the wing structure that allowed him to solve analytically for the lift distribution that gives a minimum induced drag for a different set of constraints. This solution included other indirect assumptions on different components of weight. Later, Hunsaker, Phillips and Joo [21] pointed out that the set of constraints Prandtl used in 1933 [17] could be relaxed without losing the ability to solve for the lift distribution corresponding to the minimum induced drag analytically. They arrived at the optimum lift distributions that minimize the induced drag for 3 additional types of constraint sets. Before we summarize their work, we should note that Hunsaker et al. [21] discussed both stress-limited and deflection-limited design constraints. In this work, we are only interested in stress-limited with prescribed wing loading, and this is the work described below. Other sets of constraint sets are explained in [21].

Prandtl [17] defined the bending moment distribution as

$$\tilde{M}_b = \int_{z'=z}^{b/2} \tilde{L}(z')(z'-z)dz', \quad \text{for } z \geq 0 \tag{6}$$

Note that for a steady level flight, the structural weight of the wing is not designed around the steady level conditions, as they produce the least bending moments compared to the hard-landing or maneuvering flight conditions. Also, the assumption that the bending moments are only proportional to the lift distribution is not accurate, as the sectional bending moments are directly affected by the spanwise structural and nonstructural weight distributions. Hunsaker et al. [21], modified Eq. (6) to include both structural and nonstructural weight distributions. Hence, the bending moment distributions at maneuvering or hard-landing are written as

$$\tilde{M}_b = n_a \int_{z'=z}^{b/2} \left[W \frac{\tilde{L}(z')}{L} - \tilde{W}_n(z') - \tilde{W}_s(z') \right] (z' - z) dz', \quad \text{for } z \geq 0 \tag{7}$$

where n_a is either the loading factor n_m in case of maneuvering, or n_g in case of hard-landing. Depending on the absolute value of Eq. (7), evaluated at both maneuvering and hard-landing, the greater bending moment provides the minimum structural weight required to support the wing stresses. Yet, both bending moment distributions need to be considered when designing for the optimal weight distribution that supports both. In this reoccurring recursive dependency, where the weight distribution is a function of the bending moment distributions which, in turn, depend on the weight distribution, an iterative procedure is one way to solve for both distributions. However, Hunsaker et al. [21] suggested a nonstructural weight distribution that provides an analytical solution given by

$$\tilde{W}_n(z) = (W - W_r) \frac{\tilde{L}(z)}{L} - \tilde{W}_s(z) \tag{8}$$

Substituting Eq. (8) into Eq. (7) for both maneuvering and hard-landing and equating the resulting two equations yields a root weight

$$W_r = \frac{n_g - 1}{n_m + n_g} W \tag{9}$$

Using the new W_r from Eq. (9) in Eq. (8) and Eq. (7), we get

$$\left| \tilde{M}_b(z) \right| = \kappa_W W_r \int_{z'=z}^{b/2} \frac{\tilde{L}(z')}{L} (z' - z) dz', \quad \text{for } z \geq 0 \tag{10}$$

$$\kappa_W = \begin{cases} n_m, & W_r \geq \dfrac{n_g - 1}{n_g + n_m} W \\ (n_g - 1) \dfrac{W}{W_r} - n_g, & W_r < \dfrac{n_g - 1}{n_g + n_m} W \end{cases} \tag{11}$$

Equation (9) defines the optimal weight distribution that minimizes the maneuvering and hard-landing bending moment distributions that are described by Eqs. (10) and (11). Using the definitions of maximum allowable stress, specific weight, area moment of inertia for a rectangular beam, and Eqs. (10) and (11), the total structural weight can be written as

$$W_s = \frac{2\kappa_W W_r}{S_b} \int_{z=0}^{b/2} \int_{z'=z}^{b/2} \frac{\tilde{L}(z')}{L} (z' - z) dz' dz; \; S_b \equiv \frac{C_\sigma (t_{max}/c) c(z) \sigma_{max}}{\gamma}, \; C_\sigma \equiv \frac{2I(h/t_{\max})}{Ah^2} \tag{12}$$

Besides being limited to stress-limited wing design, we notice from Eq. (12) that this structural weight applies only to spanwise symmetric wing loading. In addition, following Prandtl's analytical solution for minimum induced drag [17] enforces the constraints of constant wing chord and thickness, since Prandtl [17] derived it assuming a proportionality factor, S_b, that is independent of spanwise coordinate, z. Hence, for a rectangular wing with symmetric spanwise loading, the stress-limited wing structural weight is proportional to Prandtl's solution [17]. The total structural weight can then be deduced as

$$W_s = \frac{\kappa_W W_r b^2}{32 S_b}\left(1 + B_3\right) \tag{13}$$

Looking at the induced drag definition in Eq. (5), for a fixed total weight and wingspan, setting the Fourier coefficients, B_n, to zero, for all n >1, reduces the induced drag and produces the elliptic lift distribution. However, for the same total weight but with a varying wingspan, allowing B_3 to take a negative value, while setting the remaining B_n to zero, for all n >1, yields less induced drag than the elliptic lift distribution. Furthermore, since the weight is kept constant, the negative B_3 gives a larger wingspan for the given structural weight. Rearranging Eq. (13) for b^2 and substituting the resulting wingspan into Eq. (5) yields

$$D_i = \frac{W^2}{S_b W_s}\frac{\kappa_W W_r}{16\pi\rho V_\infty^2}\left(1 + B_3 + 3B_3^2 + 3B_3^3\right) \tag{14}$$

Looking at Eq. (14), it's evident that the induced drag for a wing with a prescribed structural, root and total weight, in steady level flight, varies with B_3 coefficient. The induced drag, as defined in Eq. (14), for fixed total weight and S_b and a varying wingspan, requires finding the value of B_3 that satisfies the following equation:

$$\left(1 + 3B_3\right)^2 = 0 \tag{15}$$

Using the solution for Eq. (15) in Eq. (4), we conclude that for a given wing weight and S_b, the induced drag is minimized for the lift distribution given by

$$\tilde{L}(\theta) \;=\; 2A_1\rho V_\infty^2 b\left[\sin(\theta) - \frac{1}{3}\sin(3\theta)\right];\;\; B_2 = 0;\;\; B_3 = -1/3;\;\; B_n = 0, \text{for } n > 3 \tag{16}$$

where

$$b = \sqrt{\frac{48 S_b W_s}{\kappa_W W_r}} \tag{17}$$

and the minimum induced drag is

$$D_i = \frac{\kappa_W W_r}{18\pi\rho V_\infty^2}\frac{W^2}{S_b W_s} \tag{18}$$

Hunsaker et al. [21] pointed out that the induced drag in Eq. (18) is the optimum for a given wing weight and S_b, assuming the lift distribution is spanwise symmetric and positive all over the semispan.

Another constraint introduced in the previous analysis is the constant chord and thickness, enforced by the independence of S_b with respect to the spanwise coordinate, z. Rather than constraining the chord, holding the wing loading constant is a common practice corresponding to aircraft speed requirements. Holding the wing loading constant in a stress-limited design of a rectangular wing with the proposed weight distribution in Eq. (8) and an all-positive spanwise symmetric lift distribution, Hunsaker et al. [21] used the definitions of the planform area, S_b and the structural weight in Eq. (13) to redefine the induced drag in Eq. (5) as a function of B_3, independent of the wingspan as

$$D_i = \frac{2\left(1+3B_3^2\right)}{\pi\rho V_\infty^2}\left[\frac{\left(1+B_3\right)\gamma\left(W/S\right)}{32C_\sigma\left(t_{max}/c\right)\sigma_{max}}\frac{\kappa_W W_r W^2}{W_s}\right]^{2/3} \tag{19}$$

Solving for the B_3 value that minimizes the induced drag for a fixed wing loading, Hunsaker et al. [21] arrived at a lift distribution as follows

$$\tilde{L}(\theta) = 2A_1\rho V_\infty^2 b\left[\sin(\theta) - 0.13564322\sin(3\theta)\right]; \qquad B_3 = -3/8 + \sqrt{9/64 - 1/12} \tag{20}$$

where $B_2 = 0$ and $B_n = 0$ for $n > 3$ as before. The corresponding wingspan becomes

$$b = \sqrt[3]{\frac{32C_\sigma\left(t_{max}/c\right)\sigma_{max}}{0.86435678\gamma\left(W/S\right)}\frac{W_s W}{\kappa_W W_r}} \tag{21}$$

and the induced drag for stress-limited constant weight and wing loading is then defined as

$$D_i = \frac{2.11039450}{\pi\rho V_\infty^2}\left[\frac{0.86435678\gamma\left(W/S\right)}{32C_\sigma\left(t_{\max}/c\right)\sigma_{\max}}\frac{\kappa_W W_r W^2}{W_s}\right]^{2/3} \tag{22}$$

Comparing the induced drag in Eqs. (22) and (19) with that corresponding to the elliptic lift distribution [12-14] and Prandtl's lift distribution in 1933 [17], Hunsaker et al. [21] found that the lift distribution corresponding to the constant wing loading and weight in Eq. (22) reduces the induced drag by 4.25 percent over the elliptic lift distribution while allowing the wingspan to increase by 4.98 percent. On the other hand, Prandtl's 1933 lift distribution [17]

increases the induced drag by 1.75 percent over the elliptic lift distribution and allows an increase of 14.5 percent in the wingspan for the same total weight.

Building on Hunsaker et al.'s work [21], and using the definition of induced drag, Eq. (19) can be rearranged to give

$$\frac{D_i}{\frac{1}{2}\rho V_\infty^2 S} = \frac{\left(1+3B_3^2\right)\left(1+B_3\right)^{2/3}}{\pi}\left[\frac{\kappa_W}{32C_\sigma S\left(t_{max}/c\right)}\frac{W_r}{W_s}\frac{\gamma\sqrt{S}}{\sigma_{max}}\right]^{2/3}\frac{W^2}{\left(\frac{1}{2}\rho V_\infty^2 S\right)^2} \tag{23}$$

Notice that for steady level flight, the total lift is equal to the total weight of the aircraft. The drag coefficient from Eq. (23) can then be defined in terms of lift coefficient and the Fourier coefficient B_3

$$C_{D_i} = \frac{C_L^2}{\pi}\left[\frac{\kappa_W}{32C_\sigma\left(t_{max}/c\right)}\frac{W_r}{W_s}\frac{\gamma}{\sqrt{S}\,\sigma_{max}}\right]^{2/3}\left(1+3B_3^2\right)\left(1+B_3\right)^{2/3} \tag{24}$$

Figure 1 shows the two non-dimensional functions of B_3 in Eqs. (14) and (24) proportional to induced drag as they vary with B_3 values. From the definition of the total drag for subsonic speeds and Eq. (24), we can define the total drag coefficient as:

$$C_D = C_{D_p} + \frac{C_L^2}{\pi}\left[\frac{\kappa_W}{32C_\sigma\left(t_{max}/c\right)}\frac{W_r}{W_s}\frac{\gamma}{\sqrt{S}\,\sigma_{max}}\right]^{2/3}\left(1+3B_3^2\right)\left(1+B_3\right)^{2/3} \tag{25}$$

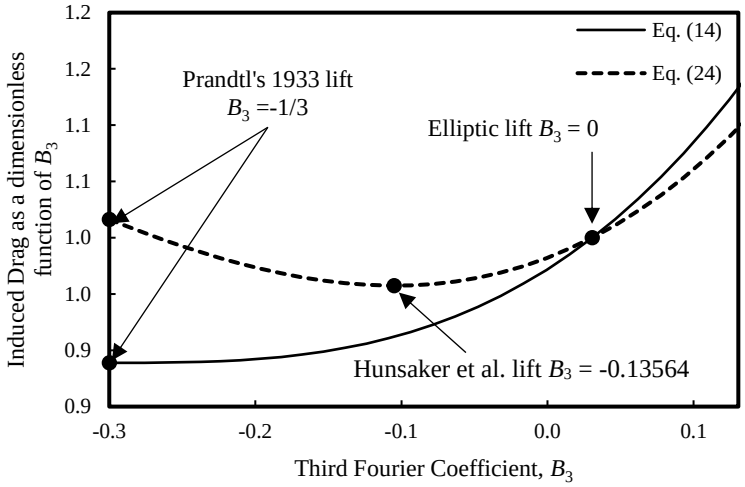

Fig. 1 Variation of induced drag as non-dimensional functions of B_3

1.2. Numerical Establishment of Lift

Hunsaker et al. [21] were able to relax Prandtl's assumptions [17] to reach the optimal lift distribution for the stress-limited design of rectangular wings by restricting the non-structural weight distribution to Eq. (8). While this

assumption helped arrive at a closed-form solution for the lift distribution on a wing with minimum induced drag, it's hardly incorporated in aircraft design in practice.

For a given lift and non-structural weight distributions, the wing structure required to support the resulting bending moments imposes bending moments itself that need to be accounted for as well. This creates a recursive dependency between the bending moments and the wing structural weight that can only be solved for iteratively. The non-structural weight distribution described in Eq. (8) decouples the bending moments and structural weight definitions and thus eliminates the need for an iterative solution. A non-structural weight distribution following Eq. (8) is seldom used in aircraft industry. Taylor, Hunsaker and Joo [22] proposed an algorithm that allows for arbitrary non-structural weight distributions and planforms. Taylor et al.'s [22] algorithm uses the same relations used by Hunsaker et al. [21] except for Eq. (8) and any planform relations, as Taylor et al. [22] extended their algorithm to allow for any unswept wing planforms as opposed to Hunsaker et al.'s [21] restriction to rectangular wings. Further details about Taylor et al.'s algorithm [22] can be found in [25].

1.2.1. Assumptions and considerations:

The structural weight algorithm considers the weight of the wing spar only when calculating the wing structural weight. The spar cross section and material properties need to be specified in advance. The algorithm allows for different cross sections as long as the area of the cross section has enough variables to comply with the number of constraints assumed but not necessarily enforced by the algorithm nor the optimizer. The algorithm also works only for unswept wings as it's based off of the lifting-line theory. The algorithm assumptions can be summarized as below:

1. The wing is unswept.
2. The wing structural weight is assumed to be the wing spar's weight only. The bending moments are supported by the spar alone. The effect/contribution of the wing skin and other wing structures is only considered as non-structural weight.
3. The wing is assumed to be in pure bending.
4. The spar cross section doesn't buckle about the spar's longitudinal axis.
5. The shape factor of the spar cross section is held constant along the spar.

1.2.2. Manufacturability

The structural weight algorithm doesn't force constraints related to the spar manufacturability and could result in section structural weights that produce high aspect ratio or non-manufacturable spar cross sections, especially with the shape factor held constant across the wingspan. For convenience, the spar cross section is set to rectangular, this is due to the simplicity of the shape factor expression of the rectangular beam compared to the box or I-beam cross sections. The rectangular beam shape factor is only a function of the beam height, whereas the box or I-beam shape factors depend on ratios of their dimensional variables, adding more constraints to the cross section calculations. The main constraints that control the manufacturability of a spar with a certain cross section is the maximum chord thickness of the section airfoil, the constant shape factor of the spar cross section along the spar and the cross section structural weight distribution specified by the algorithm. Some cross sections may not be manufacturable with the given constraints. Manufacturing and stress translation considerations can also impose constraints on the outer/inner height and/or width of the spar adding to the number of constraints the cross section has to comply with. The algorithm doesn't account for buckling of the cross section. For instance, running the algorithm with example wing-loading, non-structural weights and flight conditions along with the constant shape factor constraint, the resulting sectional structural weight values for both wings tend to be very small at both ends of the wing, as shown in Fig 2, producing spar cross sections of very high aspect ratios that don't provide enough inertia to resist bending in practical loading situations.

For small structural weight at a given section, manufacturing becomes a concern, and additional "unnecessary" spar weight might be needed to reach a manufacturable spar. This adds to the non-structural weight which might require running the algorithm again with the added spar weight as part of the wing non-structural weight. Having different wingspans for elliptic and optimal lift distributions means the length of this added beam differs for each wing resulting in different amount of added weight to each wing. To keep the non-structural weight constant across both lift distributions, the weight of the beam added to the optimal wing (the larger span) is evaluated and added to the total non-structural weight for both wings. This non-structural weight is then used as the initial non-structural weight guess in an optimizer that iterates on non-structural weights and spans of both lift distributions till the non-structural weight converges. A possible way around adding nonstructural weight to the spar is to quantify the support provided by the wing structure that the wing-structure algorithm does not account for (skin and ribs) and check if they are sufficient to support the small bending moment values at the tips of the wing. The analysis above focuses on reducing the induced

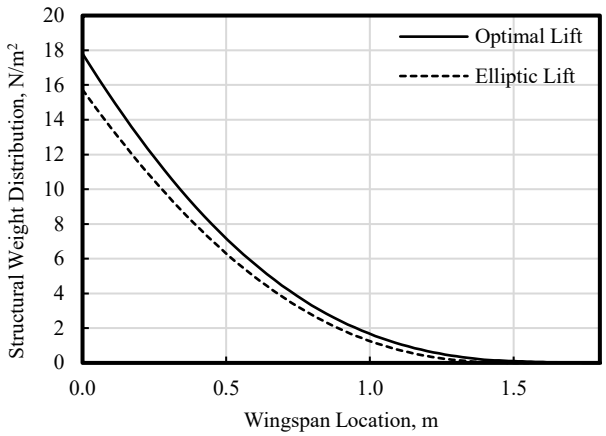

Fig. 2 Example structural weight distributions associated with the elliptic and optimal lift distributions

drag, which at low speeds dominates and becomes a function of the square of the lift. However, the fact that the optimum lift distribution for a minimum induced drag requires twisting the wing aerodynamically and/or geometrically, and consequently, contributes to the parasitic drag component, suggests looking at the effects of such lift distributions on the parasitic and total drag. Whereas the induced drag can be evaluated analytically, the parasitic drag can only be evaluated numerically for a given twist distribution.

This work uses a numerical lifting-line algorithm and numerical methods to study the effect of the optimum lift distribution, obtained using Taylor et al.'s [22] wing-structure algorithm as discussed above, on the parasitic component of drag. Minimizing the induced drag is favorable, but if the new lift distribution requires a wing twist that increases the parasitic drag enough to cancel the benefits of the induced drag reduction, then wings with elliptic loading have the advantage of more convenient and well-established manufacturing and design processes. For convenience, throughout the rest of the paper, the lift distribution obtained utilizing Taylor et al.'s wing structure algorithm [22] is referred to as the optimal or optimum lift distribution.

The next chapter discusses the optimization procedure used to reach the optimal lift distribution with the wing-structure algorithm as the objective function. It also discusses the constraints and assumptions of the wing-structure. Chapter 3 discusses the aerodynamic data used to define the twist and obtain the parasitic drag in MachUp. Chapter 4 describes the optimization process for the section twist that produces optimal and elliptic lift distributions, and Chapter 5 discusses the results. Conclusion and future work follow in Chapter 6.

CHAPTER TWO

OPTIMAL LIFT DISTRIBUTION

Taylor et al.'s numerical algorithm [22], introduced in the last section in Chapter 1, predicts the wing structural weight required to support the bending moments corresponding to a given wingspan, non-structural weight distribution and lift distribution. But as the wingspan and chord can vary while the wing loading is held constant, the structural weight has to vary along to attune to the changes in area. Coupling the wing-structure algorithm with an optimizer, and fixing the non-structural weight distribution and wing loading, the lift distribution and wingspan can then be varied to reach a minimum induced drag. Lifting-line theory is used in predicting the induced drag for a given lift distribution and wingspan. The optimal lift distribution and wingspan associated with the minimum induced drag for the prescribed non-structural weight and wing loading are found following the process described below:

1. For a given total non-structural weight, the elliptic lift distribution and wingspan are defined.
2. The wing structure algorithm [22] is used to calculate the structural weight required to support the resulting bending moments from the elliptic lift distribution and wingspan.
3. The given non-structural weight and wing loading are held constant while the wingspan and lift distribution are varied by the optimizer.
4. For every lift distribution and wingspan suggested by the optimizer, the corresponding structural weight and induced drag are calculated using the wing structure algorithm and lifting-line based algorithm.
5. When the user-defined convergence criterion is met, the optimizer stops and returns the corresponding lift distribution as the optimal lift distribution for the given non-structural weight and wingspan.

As the structural weight and wingspan are allowed to vary when solving for the optimal lift distribution, the area must change in order to keep the wing loading constant. The required change in wingspan is not constrained by the area and vice versa. This leaves the possibility open for the chord to change to be able to reach the required area and wingspan values for optimal lift distribution with a constant wing loading. Note that different chords lead to different Reynold's numbers for constant velocity.

2.1 BluJay

BluJay is a UAV developed by AggieAir lab[1] for aerial imagery for water and agricultural purposes. Its non-structural weight and flight conditions are used in this analysis, and its original wingspan is used as a baseline design. Taylor et. al's wing-structure algorithm [22] is used as an objective function inside an optimizer as described above to obtain the optimal lift distribution for BluJay. The structural weights for both lift distributions, as well as the structural weight distribution, chord and wingspan associated with the optimal lift distribution, are also calculated using Taylor et al.'s wing structure algorithm. Table 1 shows the optimal and elliptic lift distribution wing specifications. Note that the spar material (carbon fiber) and cross section airfoil (Clark-Y) of BluJay are not used in this design. Instead, Aluminum 6061 and parabolic flap representation of NACA XX12 airfoil series are used for easier stress and camber calculations. The optimal lift distribution Fourier coefficients for BluJay obtained utilizing the wing-structure algorithm [22] are found in Table A.1 in Appendix A. Figures 2 and 3 show the resulting structural weight distributions and lift distributions for both wings respectively.

Table 1 Baseline wing design for elliptic and optimal lift distributions

WING PROPERTIES	**ELLIPTIC LIFT**	**OPTIMAL LIFT**
Wing area (m^2)	0.7398530523	0.7524890035
Wing span (m)	3.10896	3.625870497
Chord length (m)	0.23797445	0.20753334
Wing loading (N/m^2)	179.8915278	
SPAR PROPERTIES		
Max tensile stress (Al 6061) (Pa)	2.76E+08	
Height/thickness	0.9	
Specific weight (N/m^3)	26487	
Beam type	Rectangular	
LOAD LIMITS		
Hard landing/Maneuvering (g)	20	
WEIGHT		
Non-structural weight (N)	118.6315275	
Non-structural distribution type	Even	
FLIGHT CONDITION		
Density (Kg/ m^3)	1.223	
Cruise velocity (m/s)	19.46607846	
C_L	0.7763495571	
Re	3.17E+05	2.77E+05

[1] *http://aggieair.usu.edu/uav_service_center/platforms_sensors*

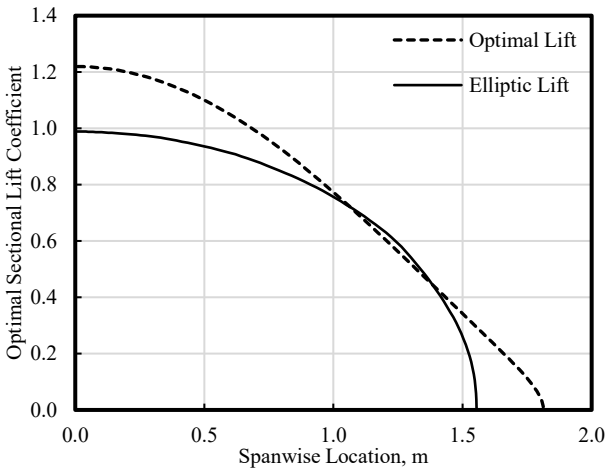

Fig. 3 Elliptic and optimal lift distributions for lujay

CHAPTER THREE

PARABOLIC FLAP AIRFOIL

To calculate the parasitic drag on a wing with a given lift distribution, lifting-line theory is used to obtain the section twist from the lift distribution. This requires the cross-section airfoil aerodynamic coefficients to be known as a function of the angle of attack. Calculating the parasitic drag requires the parasitic drag coefficient to also be defined at each wing section. XFOIL, a Fortran-based airfoil analysis and design software for both inviscid and viscous settings [26], is used to obtain the coefficients of NACA XX12 airfoil series at various angle of attack. To get a smooth and continuous camber distribution for the airfoils used, instead of using the 4-digit NACA series airfoils directly with XFOIL, a parabolic flap [27], hinged at the leading edge, is utilized to create the different XX12 cambers, starting from 0012 airfoil, by controlling the flap deflection. Aerodynamic coefficients for each flap deflection are evaluated at a range of angles of attack using a three-stage python script [27]. Stage one runs multiple cases of XFOIL over a range of angles of attack for each flap deflection representing a higher camber of XX12 airfoil. The second stage fits a polynomial to the aerodynamic coefficients of each flap deflection as a function of angle of attack according to user-specified polynomial degrees and types and the third stage fits a polynomial to the equation coefficients of the second-stage fit curve. The fits resulting from the third stage describe the airfoil aerodynamic coefficients as a function of both angle of attack and flap deflection which makes it more convenient to use with MachUp than looking up separate functions for both variables. Further details of parabolic flap as well as the camber control by flaps and the theory the airfoil database script is based on are found in [27] and [28]. Note that the Reynold's number for the elliptically loaded wing differs from that of the wing with the optimal lift distribution due to the difference in chord lengths discussed in Chapter 2. This results in a separate aerodynamic fit coefficient database for each lift distribution, and Reynold's number, as shown in appendices B and C. Reynold's numbers associated with each lift distributions are listed in Table 1. MachUp substitutes the required angles of attack and flap deflection into a polynomial with the final stage fits to obtain the aerodynamic coefficients. For a given angle of attack and deflection, the aerodynamic coefficients are calculated using the polynomial

$$C = \sum_{j=0}^{k} \begin{cases} \sum_{i=0}^{m} a_{ki} \alpha^k \delta^i, & \text{asymmetric} \\ \sum_{i=0}^{m} a_{ki} \alpha^k \left|\delta^i\right|, & \text{symmetric} \end{cases} \tag{27}$$

where C is a general term for the aerodynamic coefficients and m and k are the degrees of the flap deflection and angle of attack polynomials. For example, using a flap deflection of 1 degrees and angle of attack of 0.05 radians, the lift coefficient at Re = 3.17E+05 is calculated using the coefficients in table B.1 as follows:

$$C_L = \begin{array}{c} [-1.06E\text{-}05 + 0.1608\delta + 6.20E\text{-}06\delta^2 - 2.64E\text{-}04\delta^3 + \\ (6.64 + 5.52E\text{-}04\delta - 4.33E\text{-}02\delta^2 - 1.08E\text{-}06\delta^3 + 7.31E\text{-}05\delta^4) * \alpha + \\ (4.57E\text{-}03 - 1.88\delta - 1.36E\text{-}04\delta^2 + 5.89E\text{-}03\delta^3) * \alpha^2 + \\ (-2.88E\text{+}01 + 4.95E\text{-}05\delta + 3.40E\text{-}02\delta^2 - 6.14E\text{-}05\delta^3 + 1.39E\text{-}03\delta^4 + 9.03E\text{-}08\delta^5 - 3.33E\text{-}06\delta^6) * \alpha^3 \\ = \mathbf{0.481875} \end{array} \quad (28)$$

CHAPTER FOUR

TWIST OPTIMIZATION

The section twist that produces a given lift distribution can be solved for either numerically or using analytical methods like lifting-line theory. Once the twist is known, numerical solutions are utilized to arrive at the parasitic drag at each wing section. MachUp, an aerodynamics analysis software based on a lifting-line numerical algorithm developed by Phillips and Snyder [29] and Optix, a python-based optimizer, are utilized to obtain the twist distributions corresponding to the given lift distributions and solve for the parasitic drag. This chapter discusses the optimization procedures and the tools used to obtain the twist that produces both lift distributions.

4.1. MachUp

MachUp is a Fortran-based, opensource, aerodynamic analysis tool based on the lifting-line numerical algorithm developed by Phillips and Snyder [29]. It also allows for viscous analysis despite the fact that it's based on lifting-line theory. To do that, MachUp uses airfoil input data in Tables B.1 and C.1 to evaluate the parasitic drag. Phillips and Synder [29] used the 3D vortex theory of lift to solve for the bound vortex strengths iteratively. MachUp uses the input airfoil data when solving for the bound vortices to get the lift as a function of the angle of attack. Once the bound vorticity at each wing section is evaluated, the angle of attack is easily calculated and used to retrieve the aerodynamic coefficients in Eq. (26). The parasitic drag components at each section is then calculated and summed about the aircraft center of gravity. Further details about MachUp features are described in [30] which also shows example applications. It's important to note that the accuracy of MachUp's estimation of the parasitic drag relies on the accuracy of the user-input airfoil data.

4.2. Optix

Optix is a Python-based, opensource, gradient-based, non-linear optimization tool. It looks for a minimum local point using line search method starting from an identity Hessian matrix and the local gradient of the objective function. It then uses the local minimum as the next design point and generates the new Hessian matrix using Broyden [31], Fletcher [32], Goldfarb [33], and Shanno [34] (BFGS) method. A user-specified convergence criterion ends the optimization process and Optix returns the final design point. It's good to note that Optix uses objective functions that are evaluated using any coding language or platform Python can integrate with. Hodson, Hunsaker, and Spall [30]

further discuss Optix code and features and use it with MachUp to solve some wing design problems. Here, we use Optix alongside MachUp to find the twist distributions that provide the optimal and elliptic lift distributions. To reach the desired sectional lift, Optix can either vary the aerodynamic or geometric twist.

4.3. Optimization Procedures:

After the structural weight optimization code described in Chapter 2 is used to find the optimal lift distribution and the airfoil database, structural weight distributions, wingspans and chords are defined for both elliptic and optimal lift distributions, MachUp and Optix are used to find the sectional twist and parasitic drag corresponding to both lift distributions. The base wing design used in the optimization is based on AggieAir's BluJay wing as discussed in Chapter 2. The first stage of this analysis is to get the section twist from the elliptic and optimal lift distributions. This is done as follows:

1. Design specifications from Table 1 are fed to MachUp along with the parabolic airfoil database.
2. An initial twist distribution is fed into Optix which runs MachUp to evaluate the corresponding initial lift distribution for the optimal/elliptic wing.
3. The objective function is the RMS error between the target optimal/elliptic lift distribution and the lift distribution associated with the initial twist guess.
4. Optix uses the RMS error in lift distributions to try to find the new line search direction and keeps changing the twist distribution accordingly until the user-specified convergence criterion is reached.

Figure 4 shows a simple diagram of the optimization process.

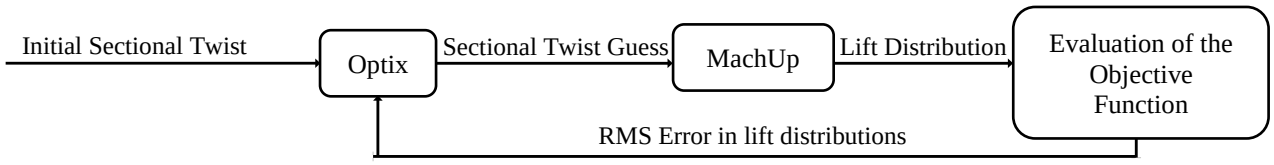

Fig. 4 Sectional twist optimization diagram

The wing section twist is defined as the relative twist of the wing section with respect to the root. This requires fixing the twist at one of the control points. This work investigates the cases where the root airfoil is fixed at each of the airfoil cambers specified in Table F.1 in Appendix F. Optix can assign any of the airfoil cambers defined by the airfoil data in appendices B and C to the variable control points. Optix can also interpolate between the discrete airfoil cambers and assign any intermediate camber value. The angle of attack is considered one of the variable degrees of

freedom in the optimization along with the 5 variable control points along the semispan since the lift coefficient is constrained. MachUp uses the sectional twist and angle of attack from every optimization case to evaluate the corresponding parasitic drag values as mentioned in Section 4.1. It also calculates the induced drag using lifting-line theory.

4.4. Grid Resolution

The section twist is defined by the optimizer at a user-defined number of points along the semispan and is linearly interpolated between these semispan locations. Optix and MachUp are used to obtain the aerodynamic twist to produce both lift distributions with a symmetric airfoil at the wing root using 2, 4, 6, and 9 actuators with 100 nodes along the semispan. Table 2 shows the parasitic drag results and percent RMS error between optimized and analytical lift distributions for both elliptic and optimal lift distributions at different number of actuators along the span. Using 4 actuators or more the parasitic drag values converge and the percent RMS error between optimized and analytical lift distributions shrinks to less than 0.15% for elliptic lift distribution and 0.35% for optimal lift distribution. Additionally, Figs. 5 and 6 compare the optimized lift distributions vs. analytical lift distributions for the case of symmetric root airfoil, 6 actuators and 100 nodes along the semispan. Note that both lift distributions match the analytical lift distributions reasonably. Figure 7 also shows the percent RMS error between the optimized and analytical lift distributions for both elliptic and optimal lift distributions. The trend lines show a reasonable convergence slope for both lift distributions using 6 actuators per semispan or higher. In this analysis, 6 control points, including the root of the wing, are used for the wing semispan. Optix and MachUp are set to calculate the twist and lift distributions at 100 nodes along the semispan.

Table 2 Grid resolution results - parasitic drag values for different control point numbers

Number of Actuators	C_{DP} (Elliptic)	C_{DP} (Optimal)	% Lift RMS Error	
			Elliptic	Optimal
2	0.03448	0.05303	10.7	23.3
4	0.03406	0.05466	5.1	7.7
6	0.03400	0.05438	0.3	0.4
9	0.03398	0.05349	0.1	0.3

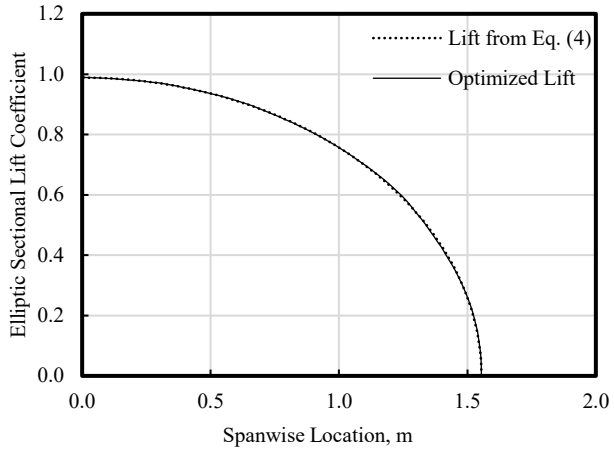

Fig. 5 Analytic and optimized elliptic lift distributions

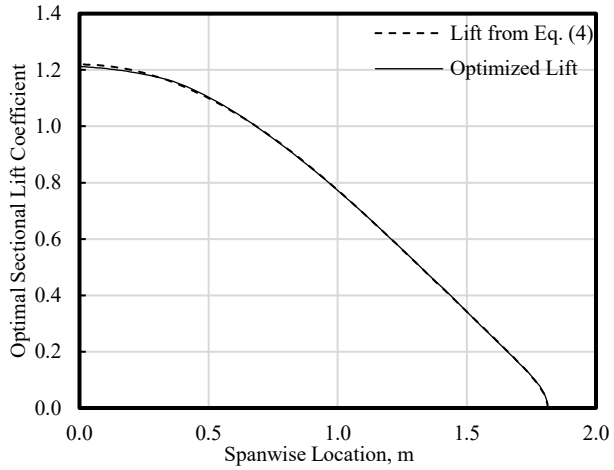

Fig. 6 Analytic and optimized optimal lift distributions

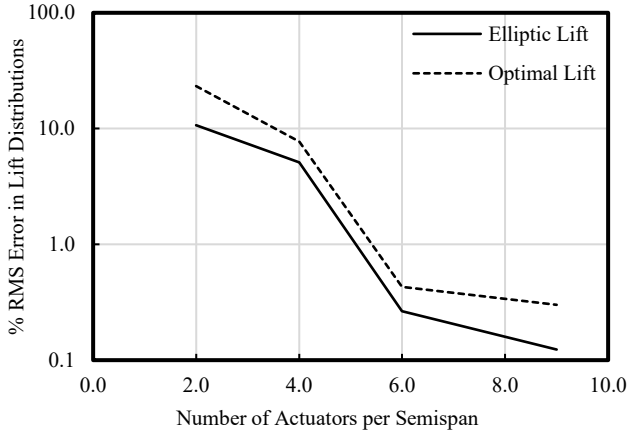

Fig. 7 Percent RMS error between optimized and analytical lift distributions

CHAPTER FIVE

RESULTS

As discussed in Chapter 4, Optix and MachUp are used to obtain the parasitic and induced drag values associated with the elliptic and optimal lift distributions for baseline specifications in Table 1. The lift is calculated at 100 nodes per semispan and Optix defines the twist at 6 control points along the semispan and linearly interpolates the twist values between these control points. A total number of 14 optimization cases are run for each lift distribution for root airfoils with 0% to 13% camber. MachUp uses the section twist and angle of attack from Optix in every optimization case to evaluate the corresponding parasitic drag values as mentioned in Chapter 4. It also calculates the induced drag using lifting-line theory. Appendix D includes MachUp input files whereas appendix E shows the Optix objective function file for the symmetric root airfoil elliptic case.

Table 3 compares the drag component values of both lift distributions for all root airfoil cases used. Note that the induced drag values are consistent for all root airfoil cases as expected since the induced drag is independent of the root airfoil. The optimal lift distribution achieves 14% less induced drag over the elliptic lift distribution for the same wing loading and non-structural weight distribution as expected, whereas the elliptic lift distribution does a better job in reducing the parasitic drag for the lower cambered root airfoil cases. However, the reduction in induced drag gained using the optimal lift distribution is encountered by nearly equal or higher increase in parasitic drag associated with the optimal lift distribution on wings with low-cambered airfoils at the root of the wing.

Lower parasitic drag values for wings with high-cambered airfoils at the root is expected as they provide higher lift at the root allowing the optimizer to choose lower angles of attack which reduces the parasitic drag. But as the camber at the root decreases, the optimizer is forced to define higher angles of attack to achieve the prescribed high lift values at the center of the wing. As shown in Table 3, starting from the case of a root airfoil of 10 % camber, the total drag associated with the optimal lift distribution is equal or less than the total drag produced on a wing with elliptic lift distribution for the same wing loading and non-structural weight distribution. However, the reduction in the total drag for such cases is not significant and lies within the accuracy tolerance of this study, but the trend line promises lower parasitic and total drag values for higher cambered root airfoils. Note that the airfoil database accuracy decreases considerably as the airfoil cambers go higher than 14% and best describes the cambers from 0% to 13%. On the other hand, using airfoil cambers in the range of 0% to 5% at the root increases the parasitic drag associated with the optimal lift distribution by more than 5% over the elliptic lift distribution's parasitic drag values. Additionally,

Table 3 Percentage difference in drag components between elliptic and optimal lift distributions

Root % Camber	% Difference		
	CD (Induced)	CD (Parasitic)	CD (Total)
13	-14.07%	-0.51%	-6.77%
12	-14.07%	5.36%	-3.87%
11	-14.07%	10.20%	-1.54%
10	-14.07%	12.66%	-0.35%
9	-14.07%	16.62%	0.07%
8	-14.07%	13.98%	0.42%
7	-14.07%	15.47%	1.28%
6	-14.07%	18.45%	2.93%
5	-14.07%	23.13%	5.53%
4	-14.07%	29.75%	9.24%
3	-14.07%	39.12%	14.59%
2	-14.08%	53.58%	22.93%
1	-14.08%	80.13%	38.35%
0	-14.31%	116.35%	59.93%

looking at Fig. 8, using a 10% camber airfoil at the root gives the minimum parasitic and total drag values associated with elliptic lift distribution. In the case of the optimal lift distribution, the 13% camber airfoil produces the lowest parasitic and total drag values compared to the studied cases. Figures 9 and 10 show the drag components as they vary with the root airfoil camber for both lift distributions. Appendix D includes the detailed drag component values for all the root airfoil cases and the corresponding angles of attack.

It's important to note that the discussed results are exclusive to the BluJay drone flight conditions and design specifications and cannot be generalized. A different aircraft needs to run similar optimization cases to study the benefits of optimal lift distribution over the elliptic lift distribution for its design and flight conditions since the optimal lift distribution that defines the twist distribution and the parasitic drag associated with the aircraft wing depends on the different weight component distributions and wing design constraints.

Although for the same root airfoil camber, optimal lift distribution doesn't offer a significant reduction in total drag over the elliptic lift distribution, the drag reduction is noticeable when the root airfoil is not constrained. Fixing the root airfoil camber has no significance in practice. Comparing an elliptically loaded wing with a symmetric airfoil at the root to a wing with optimal lift distribution and 13% camber at the root, a 12.65% reduction in total drag is achieved by utilizing the optimal lift distribution. As shown in Fig. 8, the elliptic lift distribution's minimum total drag coefficient is achieved at 10% camber at the airfoil and is about 0.0301. The 10% camber is a local minimum point when looking at the total drag in the case of elliptic lift distribution, the total drag slope is almost zero. On the

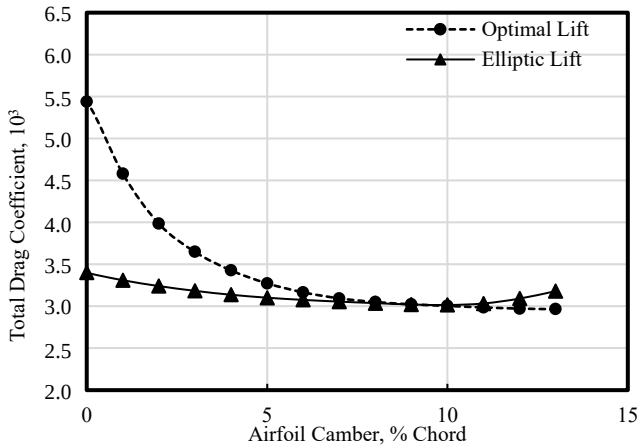

Fig. 8 Total drag of both lift distributions as a function of root airfoil camber

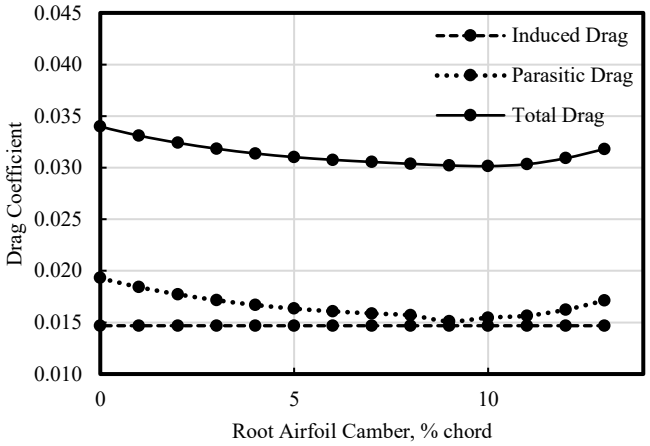

Fig. 9 Drag components associated with elliptic lift

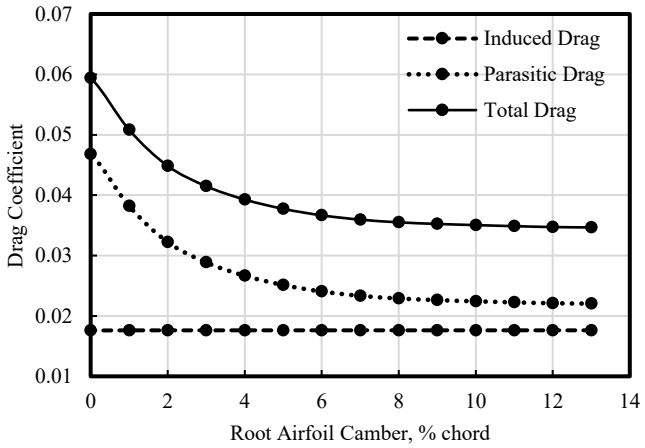

Fig. 10 Drag components associated with optimal lift

other hand, the total drag associated with the optimal lift distribution can still be further reduced below the elliptic lift distribution's minimum by increasing the root airfoil camber. This is where the benefits of the optimal lift distribution in reducing total drag might be notable. As shown from Table D.1, a wing with optimal lift distribution can achieve

only additional 2% reduction in total drag over the elliptic lift distribution's minimum total drag value. This indicates the optimal lift distribution can offer a remarkable drag reduction benefit over the elliptic lift distribution with the same non-structural weight distribution and wing loading comparing high cambered root airfoil cases in the optimal lift distribution with low cambered root airfoils for elliptic lift distribution. However, comparing minimum total drag points for both lift distributions from the cases covered in this study, optimal lift distribution doesn't offer a significant reduction in total drag. Notice that taking the accuracy level of the aerodynamics coefficients database into account and given it's a polynomial with non-zero RMS error, a 2% difference in parasitic or total drag should be considered within the accuracy margin and not seen as a significant difference in total drag values between the elliptic and optimal lift distributions.

CHAPTER SIX

CONCLUSION

It is shown that although induced drag on a wing in a steady level flight is minimized by manipulating the lift distribution along the wing, it might not necessarily reduce the total drag acting on the wing. Prandtl suggested the elliptic lift distribution as a way to minimize the induced drag in steady level flight for a prescribed weight and wingspan. He later suggested a bell-shaped lift distribution and suggested that depending on the design constraints, the lift distribution that minimizes the induced drag would differ. Hunsaker et al. suggested an optimum lift distribution, which shifts the lift towards the wing root, as a way to further reduce the induced drag than the elliptic and bell-shaped lift distributions for the constraint of prescribed wing loading. Taylor et. al further extended Hunsaker et al.'s analysis and introduced a wing structure algorithm that coupled with an optimizer solves for the optimal lift distribution for minimum drag for arbitrary wing planforms and non-structural weight distributions.

Minimizing the induced drag is desirable as it's proportional to the lift squared and dictates about 50% of the total drag in a steady level flight in subsonic applications. However, changing the lift distribution on a wing necessitates modifying the wing sectional twist. Changing the wing twist alters the parasitic drag values, the other major contributor to the total drag in subsonic applications, and can compromise the benefits gained from reducing the induced drag. The effects of the elliptic lift distribution and optimal lift distribution obtained using Taylor et al.'s wing-structure algorithm on the parasitic drag values on a wing with a prescribed non-structural weight distribution and wing loading are investigated. Table A.1 in appendix A summarizes the optimal lift distribution used in this study.

The flight conditions and design specifications of Utah State University's AggieAir BluJay drone are used as a baseline design for this analysis. MachUp, an aerodynamic analysis tool based on the lifting-line numerical algorithm, is used along with Optix, a Python-based optimizer, to calculate the sectional twist, parasitic drag and induced drag associated with both the elliptic and optimal lift distributions.

The aerodynamic twist distribution is allowed to vary at only 5 control points along with the wing angle of attack inside the optimizer to achieve the prescribed lift distributions. Note that the wing root airfoil is fed to the optimizer since the twist at a wing cross section is defined as the difference between the twist at two locations along the wingspan. The twist between the control points is linearly interpolated. XFOIL, a Fortran-based airfoil analysis and design software for both inviscid and viscous settings, is used to obtain the coefficients of NACA XX12 airfoil series

at each angle of attack. To get a smooth and continuous camber distribution for the airfoils used, instead of using the 4-digit NACA series airfoils directly with XFOIL, a parabolic flap, hinged at the leading edge, is utilized to create the different XX12 cambers, starting from 0012 airfoil, by controlling the flap deflection. The final airfoil database is a polynomial that relates the aerodynamic coefficients of the parabolic flap NACA XX12 to the angle of attack and parabolic flap deflection. This airfoil database is used to define the sectional twist that produces both lift distributions used in this study.

The airfoil at the wing root is varied from a 0% to 13% camber and MachUp and Optix are used to predict the wing sectional twist corresponding to both lift distributions for each root airfoil case. MachUp is utilized afterwards to retrieve the induced and parasitic drag values associated with the twist distribution predicted.

It's shown that the optimal lift distribution reduces the induced drag by almost 14% over the elliptic lift distribution over a wing with prescribed wing loading and non-structural weight distribution. It's also shown that in the cases of optimal lift distribution where low-cambered airfoils are used at the wing root, the optimizer forces a high angle of attack to be able to achieve the high optimal lift values at the root. This increases the parasitic drag and not only cancels out any benefits gained from the induced drag reduction, but actually increases the total drag significantly compared to the values of the total drag acting on the elliptic wing with the same root airfoil. Table 2 briefs the relative drag reductions and gains of the elliptic and optimal lift distributions for all the root airfoil cases. When high-cambered airfoils are defined for the root airfoil (10% camber or higher) the optimizer doesn't need to impose a high angle of attack to make up for the high lift values at the wing center. This produces less parasitic drag and can achieve a small reduction in total drag over the elliptic lift distribution like in the case of 13% camber root airfoil for both lift distributions. Total drag reduction gained from the optimal lift distribution over the elliptic lift distribution for the same root airfoil camber is possibly negligible and within the study accuracy tolerance, which implies that for the aircraft investigated, for the same root airfoil camber, the best scenario for the optimal lift distribution is producing the same total drag values as the elliptic lift distribution. Detailed drag values for both lift distributions are summarized in Table F.1 in appendix F.

Looking at the minimum total drag values that both lift distributions can achieve when the root airfoil camber is not constrained, the optimal lift distribution does a slightly better job in reducing the total drag than the elliptic lift distribution. The minimum total drag value the elliptic drag can achieve is shown to be about 0.0301 at a root airfoil camber of about 10%. Going below or above this point increases the total drag value for an elliptically loaded wing.

The optimal lift distribution's minimum point is not obtained in this study, but the trend line shows further expected reduction in the total drag for root airfoil cambers higher than 13%. Optimal lift distribution produces the elliptic lift distribution's minimum total drag value at a root airfoil camber of 10% as well. But the total drag trend line for the optimal lift distribution goes further below this value as the root airfoil cambers increase. Table F.1 shows that the optimal lift distribution doesn't go far below the elliptic lift's minimum total drag value with the lowest point at 13% camber at the root with 2% lower total drag than the minimum total drag point for elliptic lift.

The results are exclusive to BluJay non-structural weight, wingspan and flight conditions. Different aircraft might experience different values for induced and parasitic drag when loaded "optimally". Optimal lift varies with non-structural weight distributions and flight conditions and can produce different total drag performance when applied to different aircraft and flight conditions.

5.1. Limitations and Future Work Recommendations

This work has only investigated the case of aerodynamic twist. A next step for this is to allow the optimizer to vary the geometric twist as well for the same lift distributions. This work was also limited to the elliptic lift distribution and the optimal lift distribution based on Taylor et al.'s wing structure algorithm in Table A.1. It's essential to generate a range of lift distributions where B_n sweep the positive symmetric lift distribution range and investigate the corresponding total and parasitic drag values across the whole range. This might give an insight on what the optimum lift distribution that reduces the total drag, rather than just the induced drag component, looks like.

REFERENCES

[1] US Energy Information Administration, "Annual Energy Outlook 2018," URL: https://www.eia.gov/outlooks/aeo/pdf/AEO2018.pdf

[2] Bureau of Transportation Statistics, "Airline Fuel Cost and Consumption (U.S. Carriers - Scheduled)," [online database], URL: https://www.transtats.bts.gov/fuel.asp

[3] Bushnell, D. M., "Aircraft drag reduction a review," *Proceedings of The Institution of Mechanical Engineers Part G-journal of Aerospace Engineering*, Vol. 217.

[4] Lin, J. C., Whalen, E. A., Eppink, J. L., Siochi, E. J., Alexander, M. G., Andino, M. Y., "Innovative Flow Control Concepts for Drag Reduction," AIAA 2016, AIAA SciTech Forum and Exposition; 4-8 Jan. 2016; San Diego, CA; United States.

[5] Spalart, P. R., McLean, J. D., "Drag reduction: enticing turbulence, and then an industry," Phil. Trans. R. Soc. A (2011) 369, 1556–1569. doi:10.1098/rsta.2010.0369.

[6] Henderson, W. and Holmes, B., "Induced Drag - Historical Perspective," SAE Technical Paper 892341, 1989, https://doi.org/10.4271/892341.

[7] Goldhammer, M. I., and Plendl, B. R., "Surface Coatings and Drag Reduction," *Aero Magazine,* QTR_01-13, [online magazine], URL: http://www.boeing.com/commercial/aeromagazine/articles/2013_q1/pdf/AERO_2013q1.pdf

[8] Kroo, I., "DRAG DUE TO LIFT: Concepts for Prediction and Reduction," *Annu. Rev. Fluid Mech.,* 2001. 33:587–617.

[9] Chanute O. 1998 (1894). *Progress in Flying Machines*. Mineola, NY: Dover. 308 pp.

[10] Lilienthal O. 1889. *Der Vogelflug als Grundlage der Fliegekunst*. Berlin: R. Gaertners Verlag. Transl. by AW Isenthal, 1911. *Birdflight as the Basis of Aviation*. London, UK: Longmans, Green, & Co. 1911. 142 pp.

[11] Lanchester FW. 1907. *Aerodynamics*. London: Constable.

[12] Prandtl, L., "Theory of lifting surfaces," *NACA TN 9, Natl. Advis. Comm. Aeronaut.,* Hampton, Va. 1918. (From Tech. Ber.)

[13] Prandtl, L., "Tragflügel Theorie," *Nachrichten von der Gesellschaft der Wissescheaften zu Göttingen,* Geschäeftliche Mitteilungen, Klasse, 1918, pp. 451-447.

[14] Prandtl, L., "*Applications of Modern Hydrodynamics to Aeronautics*," NACA 116, June 1921.

[15] Rokhsaz, K. A brief survey of wing tip devices for drag reduction. SAE paper 93-2574, 1993.

[16] Spillman, J. J. Wing tip sails: progress to date and future developments. *Aeronaut. J.,* December 1987, 445-453.

[17] Prandtl, L., "Über Tragflügel kleinsten induzierten Widerstandes," *Zeitschrift für Flugtechnik und Motorluftschiffahrt*, Vol. 11, 1933, pp. 305-306.

[18] Klein, A., and Viswanathan, S. P., "Minimum Induced Drag of Wings with Given Lift and Root-Bending Moment," *Zeitschrift fur Angewandte Mathematik und Physik*, Vol. 24, 1973, pp. 886-892.

[19] Gopalarathnam, A., and Norris, R. K., "Ideal Lift Distributions and Flap Angles for Adaptive Wings," *Journal of Aircraft*, Vol. 46, No. 2, 2009, pp. 562-571.

[20] McGeer, T., "Wing Design for Minimum Drag with Practical Constraints," *Journal of Aircraft*, Vol. 21, No. 11, 1984, pp. 879-886.

[21] Hunsaker, D. F., Phillips, W. F., and Joo, J. J., "Designing Wings with Fixed Twist for Minimum Induced Drag," AIAA 2017-1419, *55th AIAA Aerospace Sciences Meeting*, AIAA SciTech Forum, Grapevine, Texas, 9-13 January 2017.

[22] Jeffrey D. Taylor, Douglas F. Hunsaker, and James J. Joo. "Numerical Algorithm for Wing-Structure Design", *2018 AIAA Aerospace Sciences Meeting*, AIAA SciTech Forum, (AIAA 2018-1050)

[23] Kutta, M. W., "Auftriebskräfte in Strömenden Flüssigkeiten," *Illustrierte Aeronautische Mitteilungen*, Vol. 6, 1902, p.133.

[24] Joukowski, N. E., "Sur les Tourbillons Adjionts," *Travaux de la Section Physique de la Societe Imperiale des Amis des Sciences Naturales*, Vol. 13, No. 2, 1906.

[25] Taylor, J. D., "Methods for the Aerostructural Design and Optimization of Wings with Arbitrary Planform and Payload Distribution," (2018). All Graduate Theses and Dissertations. 6909

[26] Drela, M., "XFOIL: An Analysis and Design System for Low Reynolds Number Airfoils," *Conference on Low Reynolds Number Airfoil Aerodynamics*, University of Notre Dame, June 1989.

[27] Montgomery, Z. S., Hunsaker, D. F., and Joo, J. J., "A Methodology for Optimal Roll Control of Morphing Aircraft," AIAA SciTech Forum, 2019 AIAA Aerospace Sciences Meeting, San Diego, California, 7-11 January, SUBMITTED.

[28] Hunsaker, D. F., Reid, J., Moorthamers, B., and Joo, J. J., "Geometry and Aerodynamic Performance of Parabolic Trailing-Edge Flaps," AIAA SciTech Forum, 2018 AIAA Aerospace Sciences Meeting, Kissimmee, Florida, 8-12 January 2018.

[29] Phillips, W. and Snyder, D., "Modern Adaptation of Prandtl's Classic Lifting-Line Theory," *J. Aircraft*, Vol. 37, No. 4, Jul. 2000, pp. 662-670

[30] Hodson, J., Hunsaker, D. and Spall, R., "Wing Optimization using Dual Number Automatic Differentiation in MachUp," AIAA 2017-0033, *55th AIAA Aerospace Sciences Meeting*, January 2017.

[31] Broyden, C., "The Convergence of a Class of Double-Rank Minimization Algorithms," *Journal of the Institute of Mathematics and Its Applications*, Vol. 6, 1970, pp. 76-90.

[32] Fletcher, R., "A New Approach to Variable Metric Algorithms," *Computer Journal*, Vol. 13, No. 3, 1970, pp. 317-322.

[33] Goldfarb, D., "A Family of Variable Metric Updates Derived by Variational Means," *Mathematics of Computation*, Vol. 24, No. 109, 1970, pp. 23-26.

[34] Shanno, D, "Conditioning of Quasi-Newton Methods for Function Minimization," *Mathematics of Computation*, Vol. 24, No. 111, 1970, pp. 647-656.

APPENDICES

Appendix A

Optimal Lift Distribution Fourier Coefficient Values for BluJay

Table A. 1 Non-zero Fourier coefficients for optimal lift distribution for BluJay

n	**Value**
3	-0.22288
5	0.011834
7	5.61E-04
9	-5.60E-04
11	-2.10E-05
13	1.23E-04
15	-2.85E-05
17	-3.20E-05
19	2.22E-05
21	5.00E-06
23	-1.23E-05
25	2.55E-06
27	5.18E-06
29	-3.93E-06

Appendix B

Polynomial Fit Coefficients for Re = 3.17E+05

Table B.1 Polynomial fit coefficients for XX12 NACA parabolic flap airfoil for Re = 3.17E+05

α	Deflection	C_L	C_D	C_m
C0	C0	-1.059E-05	1.361E-02	-8.397E-06
	C1	1.608E-01	1.586E-06	-1.244E-02
	C2	6.196E-06	5.123E-05	-4.226E-07
	C3	-2.635E-04	-3.167E-08	6.867E-05
	C4		9.082E-07	-1.646E-09
	C5			-1.520E-07
C1	C0	6.635E+00	-1.296E-04	2.371E-032
	C1	5.518E-04	4.858E-03	1.015E-02*
	C2	-4.327E-02	-1.143E-06	3.452E-03*
	C3	-1.079E-06	1.633E-04	-1.357E-02*
	C4	7.305E-05		1.134E-02*
	C5			-4.168E-03*
	C6			8.830E-04*
	C7			-1.165E-04*
	C8			9.705E-06*
	C9			-4.969E-07*
	C10			1.429E-08*
	C11			-1.769E-10*
C2	C0	4.572E-03	9.706E-02	4.070E-01
	C1	-1.880E+00	-2.134E-04	-4.279E-03
	C2	-1.355E-04	1.125E-02	8.536E-06
	C3	5.886E-03	-3.146E-07	
	C4		4.434E-05	
	C5		1.624E-08	
	C6		-2.762E-07	
C3	C0	-2.884E+01	-5.268E-03	3.515E+00*
	C1	4.952E-05	5.103E-01	-6.848E+00*
	C2	3.395E-02	1.351E-03	1.429E+01*
	C3	-6.141E-05	2.886E-03	-1.172E+01*
	C4	1.390E-03	-2.068E-05	5.307E+00*
	C5	9.030E-08	-3.942E-05	-1.479E+00*
	C6	-3.332E-06	7.494E-08	2.657E-01*
	C7		6.390E-08	-3.137E-02*

* Symmetric polynomial

Continue Table B.1

α	Deflection	C_L	C_D	C_m
C3	C8			2.421E-03*
	C9			-1.174E-04*
	C10			3.246E-06*
	C11			-3.896E-08*
C4	C0		8.027E+00	1.748E-02
	C1		2.550E-02	-2.460E+00
	C2		9.220E-02	
	C3		-4.726E-04	
	C4		-1.277E-03	
	C5		1.879E-06	
	C6		2.284E-06	
C5	C0			-1.804E+01*
	C1			3.218E+02*
	C2			-7.369E+02*
	C3			6.589E+02*
	C4			-3.172E+02*
	C5			9.214E+01*
	C6			-1.708E+01*
	C7			2.067E+00*
	C8			-1.626E-01*
	C9			8.011E-03*
	C10			-2.243E-04*
	C11			2.725E-06*

Appendix C

Polynomial Fit Coefficients for Re = 2.77E+05

Table C.1 Polynomial fit coefficients for 0012 NACA parabolic flap airfoil for Re = 2.77E+05

α	δ	C_L	C_D	C_m
C0	C0	1.39E-04	1.40E-02	-1.52E-05
	C1	1.60E-01	-4.83E-06	-1.22E-02
	C2	2.64E-06	5.72E-05	-4.23E-07
	C3	-2.62E-04	5.77E-08	6.78E-05
	C4		8.83E-07	9.70E-10
	C5			-1.50E-07
C1	C0	6.62E+00	-2.49E-04	3.71E-03
	C1	3.98E-04	2.12E-03	4.73E-02
	C2	-4.34E-02	1.06E-05	-6.97E-02
	C3	-3.50E-08	2.26E-04	5.71E-02
	C4	7.43E-05	9.71E-08	-2.59E-02
	C5		-2.75E-07	7.46E-03
	C6			-1.40E-03
	C7			1.73E-04
	C8			-1.40E-05
	C9			7.07E-07
	C10			-2.04E-08
	C11			2.55E-10
C2	C0	-1.28E-02	1.13E-01	4.02E-01
	C1	-1.90E+00	4.07E-06	-4.10E-03
	C2	2.44E-04	9.76E-03	8.08E-06
	C3	5.72E-03	1.56E-05	
	C4	1.20E-06	9.24E-05	
	C5	3.82E-07	-1.57E-07	
	C6		-6.96E-07	
	C7		2.71E-10	
	C8		1.06E-09	
C3	C0	-2.92E+01	1.49E-02	3.80E+00
	C1	-3.29E-02	3.82E-01	-7.09E+00
	C2	2.72E-02	-7.13E-04	1.33E+01
	C3	1.15E-03	8.85E-03	-1.09E+01
	C4	1.23E-03	-6.10E-06	5.08E+00
	C5	-9.90E-06	-9.56E-05	-1.45E+00
	C6	-2.36E-06	-2.84E-08	2.65E-01

Continue Table C.1

α	δ	C_L	C_D	C_m
C3	C7	2.71E-08	2.20E-07	-3.17E-02
	C8	-1.38E-09		2.48E-03
	C9			-1.22E-04
	C10			3.41E-06
	C11			-4.16E-08
C4	C0		9.58E+00	1.09E+00
	C1		5.53E-03	-3.27E+00
	C2		-5.11E-02	
	C3		-6.03E-04	
	C4		2.39E-03	
	C5		8.89E-07	
	C6		-2.61E-05	
	C7		-6.62E-09	
	C8		6.84E-08	
C5	C0			-2.34E+01
	C1			1.49E+02
	C2			-2.84E+02
	C3			2.29E+02
	C4			-1.01E+02
	C5			2.70E+01
	C6			-4.57E+00
	C7			5.03E-01
	C8			-3.59E-02
	C9			1.61E-03
	C10			-4.09E-05
	C11			4.52E-07

Appendix D

MachUp Input Files

D.1. MachUp Input File for Optimal Lift Optimization

```
{
"airfoil_DB": "../AirfoilDatabase",
"run": {
    "xstl" : "",
    "xforces" : "",
    "xtargetcl" : {
  "CL" : 0.7763495571,
  "maxiter": 100
},
    "distributions" : {"output" : "txt"},
    "xderivatives" : "",
    "xaerocenter" : "",
    "xreport" : {
        "fitness" : {
            "name" : "total.myairplane.CD",
            "file" : "input_forces.json"
        },
        "Cl" : {"name" : "total.myairplane.Cl", "file" :
"input_forces.json"},
        "CL" : {"name" : "CL", "file" : "input_targetCL.json"}
    },
    "xpitchtrim" : {"CL" : 0.4,"Cm" : 0.0}
},
"solver":{
  "type" : "nonlinear",
  "convergence" : 1.0e-10,
  "relaxation": 0.9
},
"plane": {
  "name": "blujayOpt",
  "CGx": -0.4,
  "CGy": 0.0,
  "CGz": 0.0
},
"reference": {
  "area": 0.7524890035,
  "longitudinal_length": 0.20753334,
  "lateral_length": 1.812935248
},
"condition": {
  "alpha": 5.85707573247733E+000,
  "beta": 0.0,
    "ground": 0.0
},
"controls" : {
    "aileron" : {
        "is_symmetric" : 0,
```

```
        "deflection" : 0.0
    },
    "elevator" : {
        "is_symmetric" : 1,
        "deflection" : 0.0
    }
},
"wings": {
  "wing_1" : {
    "ID": 1,
    "side": "both",
    "connect": {
      "ID": 0,
      "location": "root",
      "dx" : 0.0,
      "dy" : 0.0,
      "dz" : 0.0,
           "yoffset" : 0.0
    },
    "span": 1.812935248,
    "sweep": 0.0,
    "dihedral": 0.0,
    "mounting_angle": 0.0,
    "root_chord": 0.20753334,
    "tip_chord":  0.20753334,
    "airfoils" : {"FinalDBOpt":""},
    "af_ratio_file" : "afratio.json",
    "washout" : 0.0,
    "washout_file": "twistfile.json",
    "grid": 100,
        "control" : {
            "span_root" : 0.0,
            "span_tip" : 0.0,
            "chord_root" : 0.0,
            "chord_tip" : 0.0,
            "is_sealed" : 1,
            "mix" : {
                "aileron" : 0.0,
                "elevator" : 0.0
            }
        }
  }
}
}
```

D.2. MachUp Input File for Optimal Lift Optimization

```
{
"airfoil_DB": "../AirfoilDatabase",
"run": {
    "xstl" : "",
    "xforces" : "",
    "xtargetcl" : {
  "CL" : 0.7763495571,
  "maxiter": 100
},
    "distributions" : {"output" : "txt"},
    "xderivatives" : "",
    "xaerocenter" : "",
    "xreport" : {
        "fitness" : {
            "name" : "total.myairplane.CD",
            "file" : "input_forces.json"
        },
        "Cl" : {"name" : "total.myairplane.Cl", "file" :
"input_forces.json"},
        "CL" : {"name" : "CL", "file" : "input_targetCL.json"}
    },
    "xpitchtrim" : {"CL" : 0.4,"Cm" : 0.0}
},
"solver":{
  "type" : "nonlinear",
  "convergence" : 1.0e-10,
  "relaxation": 0.9
},
"plane": {
  "name": "blujayOpt",
  "CGx": -0.4,
  "CGy": 0.0,
  "CGz": 0.0
},
"reference": {
  "area": 0.7398530523,
  "longitudinal_length": 0.23797445,
  "lateral_length": 1.55448
},
"condition": {
  "alpha": 5.85707573247733E+000,
  "beta": 0.0,
    "ground": 0.0
},
"controls" : {
    "aileron" : {
        "is_symmetric" : 0,
        "deflection" : 0.0
    },
    "elevator" : {
        "is_symmetric" : 1,
```

```
        "deflection" : 0.0
    }
},
"wings": {
  "wing_1" : {
    "ID": 1,
    "side": "both",
    "connect": {
      "ID": 0,
      "location": "root",
      "dx" : 0.0,
      "dy" : 0.0,
      "dz" : 0.0,
           "yoffset" : 0.0
    },
    "span": 1.55448,
    "sweep": 0.0,
    "dihedral": 0.0,
    "mounting_angle": 0.0,
    "root_chord": 0.23797445,
    "tip_chord":  0.23797445,
    "airfoils" : {"FinalDBEll":""},
    "af_ratio_file" : "afratio.json",
    "washout" : 0.0,
    "washout_file": "twistfile.json",
    "grid": 100,
       "control" : {
           "span_root" : 0.0,
           "span_tip" : 0.0,
           "chord_root" : 0.0,
           "chord_tip" : 0.0,
           "is_sealed" : 1,
           "mix" : {
               "aileron" : 0.0,
               "elevator" : 0.0
           }
       }
  }
}
}
```

Appendix E

Optix Objective Function Files

E.1. Objective Function for Elliptic Lift Distribution

```
import os
import shutil
import json
import tempfile

import math
from sklearn.metrics import mean_squared_error as mse

def evaluate(args):
    # Unpack arguments
    x = args[0]
    case_id = args[1]


    # Get the current working directory
    work_dir = os.getcwd()

    # Get the current working directory and case directory names
    orig_dir = work_dir + '/' + 'OrigFiles'
    case_dir = work_dir + '/' + str(case_id)

    # Remove existing folder with same case ID
    if os.path.exists(case_dir): shutil.rmtree(case_dir)

    # Copy original files into case directory
    shutil.copytree(orig_dir, case_dir)

    # Make the temporary directory current
    os.chdir(case_dir)

    # Generate washout input file
    twist_vars = { 'r1':  { 'c1': 0.00, 'c2': 0.0 },
                           'r2':  { 'c1': 1/5, 'c2': x[0] },
                           'r3':  { 'c1': 2/5, 'c2': x[1] },
                           'r4':  { 'c1': 3/5, 'c2': x[2] },
                           'r5':  { 'c1': 4/5, 'c2': x[3] },
                           'r6':  { 'c1': 1.00, 'c2': x[4] } }
    alpha_var = x[5]

    with open('afratio.json', 'w') as data_file:
        json.dump(twist_vars, data_file, sort_keys = True, indent = 4)

    machup_input = json.load(open('input.json'))
    machup_input['condition']['alpha'] = alpha_var

    with open('input.json', 'w') as machup_file:
        json.dump(machup_input,machup_file)


    # Execute MachUp
    # Machup Ip File: blujay
```

```
    os.system('./MachUp.out input.json > out.txt')
    ######################################################################3

    # Extract cost function from MachUp results

    z = []
    z_tmp = []
    cl = []
    cl_req = []
    cl_twist = []

    with open('input_distributions.txt') as inf:
        for line in inf.readlines()[2:201]:
            line = line.strip()
            cols = line.split(maxsplit = 15)
            cl.append(cols[13])
            z_tmp.append(cols[2])

    for item in cl:
        cl_twist.append(float(item))

    for item in z_tmp:
        z.append(float(item))

    ###
    data = json.load(open('BluJay_elliptic.json'))
    B = data['lift_distribution']['B']
    rho = data['flight']['density']
    v = data['flight']['velocity']
    c = 0.23797445
    b = data['wing']['wing_span']


    ## Lift Distribution
    Ls = []
    sigma = 0
    w = 133.0932959
    for item in z:
        n = 2
        sigma = 0
        for Bn in B:
            sigma = sigma + Bn*math.sin(n*math.acos(-2*item/b))

        Ls.append(4*w*(math.sin(math.acos(-
2*item/b))+sigma)/((math.pi*b)*0.5*rho*v*v*c))
        n = n+1

    cl_rms = math.sqrt(mse(cl_twist,Ls))

     ###############################################################################
     # Move to the original work directory and remove the temporary directory
     os.chdir(work_dir)

     return cl_rms
```

Notes:

- For Optimal Lift Distribution, the wing and aircraft specifications like the chord and weight values are switched and the same code is used.
- The file “BluJay_elliptic.json” is a JSON* file that contains the data in Table 1 for the elliptic lift distribution and a similar file for the optimal also includes the data in Table A.1.

Appendix F

Drag Component Values for Elliptic and Optimal Lift Distributions

Table F.1 Angle of attack, induced, parasitic and total drag values for elliptic and optimal lift distributions

Root % Camber	Elliptic				Optimal			
	α (Deg)	CD (inviscid)	CD (viscous)	CD (total)	α (Deg)	CD (inviscid)	CD (viscous)	CD (total)
13	-8.07E+00	1.47E-02	1.71E-02	3.18E-02	-4.60E+00	1.26E-02	1.70E-02	2.97E-02
12	-6.78E+00	1.47E-02	1.62E-02	3.09E-02	-3.30E+00	1.26E-02	1.71E-02	2.97E-02
11	-5.38E+00	1.47E-02	1.57E-02	3.03E-02	-1.90E+00	1.26E-02	1.72E-02	2.99E-02
10	-3.92E+00	1.47E-02	1.55E-02	3.01E-02	-4.35E-01	1.26E-02	1.74E-02	3.00E-02
9	-2.43E+00	1.47E-02	1.51E-02	3.02E-02	1.07E+00	1.26E-02	1.76E-02	3.02E-02
8	-9.35E-01	1.47E-02	1.57E-02	3.04E-02	2.61E+00	1.26E-02	1.79E-02	3.05E-02
7	5.53E-01	1.47E-02	1.59E-02	3.06E-02	4.19E+00	1.26E-02	1.83E-02	3.09E-02
6	2.04E+00	1.47E-02	1.61E-02	3.08E-02	5.80E+00	1.26E-02	1.90E-02	3.17E-02
5	3.51E+00	1.47E-02	1.63E-02	3.10E-02	7.48E+00	1.26E-02	2.01E-02	3.27E-02
4	4.99E+00	1.47E-02	1.67E-02	3.14E-02	9.21E+00	1.26E-02	2.17E-02	3.43E-02
3	6.47E+00	1.47E-02	1.72E-02	3.18E-02	1.10E+01	1.26E-02	2.39E-02	3.65E-02
2	7.95E+00	1.47E-02	1.77E-02	3.24E-02	1.29E+01	1.26E-02	2.72E-02	3.98E-02
1	9.42E+00	1.47E-02	1.84E-02	3.31E-02	1.51E+01	1.26E-02	3.32E-02	4.58E-02
0	1.09E+01	1.47E-02	1.93E-02	3.40E-02	1.74E+01	1.26E-02	4.18E-02	5.44E-02